JPhys Materials

PURPOSE-LED PUBLISHING™

TOPICAL REVIEW • OPEN ACCESS

A material design guideline for self-assembled vertically aligned nanocomposite thin films

To cite this article: Jiawei Song and Haiyan Wang 2025 *J. Phys. Mater.* **8** 012002

IOP Publishing J. Phys. Mater. 8 (2025) 012002 https://doi.org/10.1088/2515-7639/ad9bee

Journal of Physics: Materials

OPEN ACCESS

RECEIVED
2 June 2024

REVISED
2 September 2024

ACCEPTED FOR PUBLICATION
8 December 2024

PUBLISHED
6 January 2025

TOPICAL REVIEW

A material design guideline for self-assembled vertically aligned nanocomposite thin films

Jiawei Song[1] **and Haiyan Wang**[1,2,*]

[1] School of Materials Engineering, Purdue University, West Lafayette 47907, United States of America
[2] School of Electrical and Computer Engineering, Purdue University, West Lafayette 47907, United States of America
* Author to whom any correspondence should be addressed.

E-mail: hwang00@purdue.edu

Keywords: nanocomposites, vertically aligned nanocomposites (VANs), self-assembly, surface energy, growth mechanism

Abstract

Nanocomposite thin films, comprising two or more distinct materials at nanoscale, have attracted significant research interest considering their potential of integrating multiple functionalities for advanced applications in electronics, energy storage, photonics, photovoltaics, and sensing. Among various fabrication technologies, a one-step pulsed laser deposition process enables the self-assembly of materials into vertically aligned nanocomposites (VANs). The demonstrated VAN systems include oxide–oxide, oxide–metal, and nitride–metal VAN films and their growth mechanisms are vastly different. These complexities pose challenges in the designs, materials selection, and prediction of the resulted VAN morphologies and properties. The review examines the key roles that surface energy plays in the VAN growth and provides a generalized materials design guideline combining the two key factors of surface energy and lattice strain/mismatch, along with other factors related to growth kinetics that collectively influence the morphology of VAN films. This review aims to offer valuable guidelines for future material selection and microstructure design in the development of self-assembled VAN films.

1. Introduction

Nanocomposite thin films are composed of two or more distinct materials at the nanoscale, where one material typically forms a matrix phase and the others are dispersed within the matrix. Because of their ability to integrate multiple functionalities, these advanced materials have garnered significant research interest in fields such as electronics, energy storage, photonics, photovoltaics, sensing [1–4]. Depending on the shape of the dispersed phase, the morphology of two-phase nanocomposites can be classified into three types: (i) 0–3 particle-in-matrix, (ii) 2–2 multilayer structures and (iii) 1–3 vertically aligned nanocomposites (VANs), as shown in figures 1(a)–(c). The numbers in these classifications refer to the dimensional connectivity of the different phases. In the 0–3 particle-in-matrix morphology, isolated particles are dispersed within a continuous matrix [2, 5, 6]. The 2–2 multilayer nanocomposite consists of alternating, continuous layers of two materials, each connected in two dimensions but confined in the third [7, 8]. The 1–3 VANs feature vertically aligned structures, such as nanopillars or nanorods, embedded within a matrix [9, 10]. These aligned nanopillars offer several unique advantages over other morphologies. First, the pillar-in-matrix morphology inherently exhibits strong anisotropy due to the high aspect ratio and vertical alignment of the nanopillars, resulting in properties such as magnetic anisotropy and hyperbolic dispersion. Second, unlike traditional thin films where strain is typically induced horizontally, VANs provide a unique platform for three-dimensional (3D) strain distribution, introducing an additional degree of freedom for strain accommodation and manipulation [11]. Furthermore, the induced vertical interfaces between the two phases enable functional coupling, such as multiferroic, magneto-optical, and electro-optical coupling [12].

The fabrication of nanocomposite films can be categorized into two main approaches: top–down and bottom–up methods. Top-down methods typically start with larger structures and break them down into smaller components through techniques such as lithography, etching, laser ablation, and focused ion beam

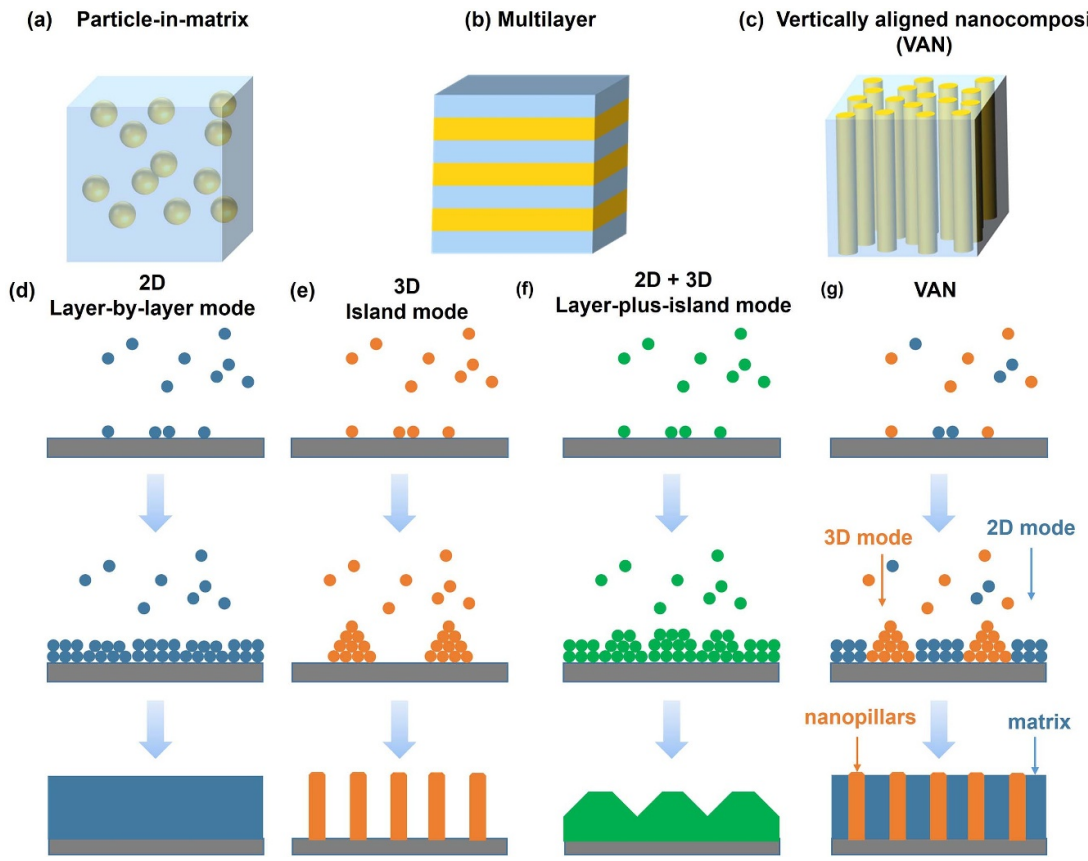

Figure 1. Schematic illustrations of (a) particle-in-matrix morphology, (b) multilayer morphology, (c) vertically aligned nanocomposite (VAN) morphology, (d) 2D layer-by-layer growth mode, (e) 3D island growth mode, (f) 2D + 3D layer-plus-island growth mode, and (g) VAN growth process combining 2D layer-by-layer mode with 3D island mode. (a), (c) [13] John Wiley & Sons. [© 2020 WILEY-VCH Verlag GmbH & Co. KGaA, Weinheim].

processing [14–19]. Bottom–up methods usually start with small components and build up to the desired nanostructure. An example of a bottom–up approach is anodized alumina templating [20–26]. Both approaches typically involve multiple steps and complex procedures, making them high-cost and time-consuming, especially for sub-10 nm nanostructures. In recent years, a more effective self-assembled approach has emerged and gained significant attention. This self-assembly technique allows for the spontaneous organization of materials into highly ordered structures without the need for external templates or seeding steps. Since self-assembly typically requires high crystallinity and a strong epitaxial growth relationship, pulsed laser deposition (PLD) has become the most commonly used method for forming VANs. In PLD, a high-energy laser is used to deposit material, providing sufficient energy to form crystalline films. Several deposition parameters, such as laser energy, laser frequency, substrate temperature, and background environment, can be adjusted to influence the growth and tune the resulting morphology. Compared to other fabrication methods, this one-step PLD process is simpler and more cost-effective for achieving nanostructured films with high crystallinity. Besides PLD, sputtering is another technique that has been used to grow VAN, such as $BiFeO_3$–$CoFe_2O_4$ and Cu_2O–Cu_4O_3 processed by magnetron sputtering [27, 28].

The concept of VANs began with the exploration of oxide–oxide systems [4, 9, 29–40], where different oxide materials were combined to create vertical nanostructures with enhanced physical properties. Early studies focused on a combination of functional oxides, such as ferroelectric BTO, ferromagnetic CFO, high-temperature superconducting $YBa_2Cu_3O_7$ [41–44]. Unlike single-phase thin films, the oxide–oxide nanocomposites can couple different functionalities within one film and therefore exhibit a range of properties simultaneously and potentially enable interactions between phases to achieve coupling effects. The second significant advancement in VAN development involved incorporating metal phase into oxide matrix, resulting in metallic nanopillars being vertically aligned within an oxide matrix, i.e. oxide–metal VANs [45–54]. These oxide–metal VAN systems expand the material selection of existing VAN designs to metals, introduce new functionalities, and enhance anisotropy in both microstructure and properties. For example, embedding plasmonic Au nanopillars inside a dielectric $BaTiO_3$ matrix creates a metal-dielectric building block, enabling a unique manipulation of light propagation with an anisotropic optical response [55–57].

Coupling ferromagnetic Co with a $BaZrO_3$ matrix has demonstrated a tunable coercive field and magnetic anisotropy [50, 52]. Recent advancements in VANs have focused on nitride-based systems, including nitride–metal and nitride–oxide systems, aiming to combine transition metal nitrides with others to form new VANs [13, 58–65]. Transition metal nitrides are known as alternative plasmonic materials since their optical properties are similar to Au but with lower optical loss and better stability [19, 66–69]. These nitride–metal VANs couple the structural robustness and unique optical properties of nitrides with the functional properties of metals, making them ideal for metamaterial design, nonlinear optics, and sensing [70–73]. Today, VANs become a powerful platform for hybrid metamaterials, coupling a broad range of materials to achieve anisotropy and coupled functionalities, with potential applications in electronics, energy storage, photonics, and beyond [9, 50, 74–79].

Understanding the growth mechanism of VANs is crucial for designing nanocomposite systems with desirable structures and properties. First, single-phase thin film formation typically follows three basic growth modes: (i) 2D layer-by-layer mode (Frank–Van der Merwe), (ii) 3D island mode (Volmer–Weber), (iii) 2D + 3D layer-plus-island mode (Stranski–Krastanov). In the 2D layer-by-layer growth mode, creating a new film surface and a film-substrate interface is energetically favorable leading materials to preferentially spread across and wet the substrate in a uniform layer (figure 1(d)). During the 3D island growth, bonding between film atoms requires less energy than bonding between film atoms and the substrate, prompting materials to cluster and form three-dimensional islands (figure 1(e)). The layer-plus-island growth mode is an intermediate case between the above two modes, where the film initially matches the substrate material but then forms islands as strain accumulates with thicker layers. Based on thermodynamics, these growth modes are governed by surface and strain energy, which determine the energetically favorable sites for nucleation and ultimate film morphology. The thermodynamic aspect of thin film growth could be described by the following equation (equation (1)). Overall thin film growth involves minimizing surface and strain energy, represented by the energy change ($\Delta\gamma$) [80]:

$$\Delta\gamma = \gamma_{\text{film}} + \gamma_{\text{interface}} - \gamma_{\text{substrate}} \tag{1}$$

where $\Delta\gamma$ represents the energy change of the system, γ_{film}, $\gamma_{\text{interface}}$, and $\gamma_{\text{substrate}}$ are the energy terms required for forming film surface, film-substrate interface and substrate surface, respectively. A high value of $\Delta\gamma$ indicates that growing the film on a substrate will significantly increase the total energy of the system, and therefore favoring island growth. Conversely, a low $\Delta\gamma$ suggests a preference for layer-by-layer growth. Typically, materials with high surface energy (large γ_{film}) or significant lattice mismatch (large $\gamma_{\text{interface}}$) compared to substrate tend to grow in island mode, whereas those with surface energies and lattice parameters similar to the substrate favor layer-by-layer growth. The growth of two-phase nanocomposite can be treated as a combination of 2D layer-by-layer mode with 3D island mode (figure 1(g)). Specifically, the pillar-in-matrix morphology is favored when the secondary phase has a higher affinity for itself than for the substrate material and therefore forms pillars by a 3D island mode, while the matrix material grows layer-by-layer. It is also noted that thin film growth generally involves the interplay between thermodynamics and kinetics parameters. Kinetics determine the rate of adatom diffusion and film growth, which are affected by deposition conditions such as substrate temperature, laser energy, and background gas pressure during PLD. The kinetic factors will be discussed later (sections 3.1) in conjunction with the review on surface energy roles.

The mechanism described above highlights surface energy and lattice parameters as critical factors in the self-assembly process of VANs. While the strain effects have been extensively covered in earlier reviews, including the epitaxy paradigm and strain compensation model [12, 29], the role of surface energy in the formation of self-assembled nanocomposite films and its impact on overall film morphology have not been thoroughly explored. This review aims to fill this gap by reviewing the self-assembly growth processes across various VAN systems, with a particular focus on the influence of surface energy on the final VAN film morphology. In this review, we begin with an overview of the surface energies of various materials commonly used in the VAN designs, including metals, oxides and nitrides and present generalized categories of all the reported VANs based on their surface energy and lattice mismatch (PART I). Next, we discuss the growth process of VAN systems composed of two materials with dissimilar surface energies and then transition to those with similar surface energies (PART II). In PART III, we expand our discussion to more complex material systems beyond two-phase nanocomposites, such as core–shell nanopillars and 3D nanostructure. Our analysis identifies the major parameters, among surface energy, crystal structure, and lattice parameters, that determine the geometry of self-assembled nanocomposite films. Finally, we propose a set of generalized guidelines for selecting materials that can be self-assembled into VAN structures, aiming to aid researchers in designing and processing nanocomposites with optimized morphologies and properties for specific applications.

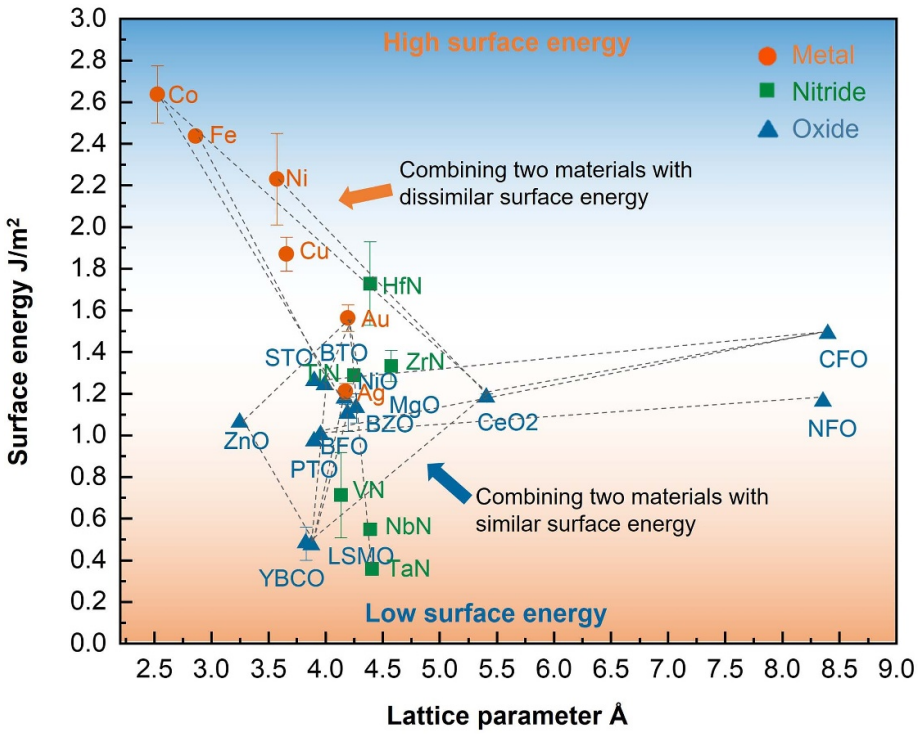

Figure 2. Summary of the relationship between lattice parameter and surface energy for metals (orange circles), oxides (blue triangles), and nitrides (green squares). The dashed lines connecting two phases represent reported VAN systems and highlight the disparities in surface energy and lattice parameter between the materials. The reported VAN systems can be categorized into two groups: those combining materials with similar surface energy (blue arrow) and those combining materials with dissimilar surface energy (orange arrow).

2. PART I: Surface energy of metals, oxides, and nitrides

Surface energy (J m^{-2}) represents the energy required to create a unit area of a surface. It reflects the tendency of a material to minimize its surface area and is influenced by various factors such as chemical bonding, atomic arrangement, and surface roughness [80–82]. During nucleation and growth, where new phases and structures form and expand, surface energy is a crucial parameter influencing the growth behavior and morphology of the films. Most metals (e.g. Au, Cu, Fe) have higher surface energies compared to those of oxides and nitrides. High surface energy in metals promotes island growth mode during thin film deposition, where atoms tend to nucleate and form small islands before coalescing into larger structures. In practice, metal films deposited on ceramic or semiconductor substrates tend to cluster or ball up to minimize their total surface and the overall system energy. Conversely, oxides and nitrides typically have lower surface energies, favoring layer-by-layer growth mode. In this mode, atoms add to the surface layer-by-layer, resulting in smoother and more uniform film growth.

Figure 2 summarizes the surface energy versus lattice parameter for various materials utilized or potentially applicable in VAN systems, with successful VAN systems indicated by dashed lines [83–86]. Most surface energy values are computational due to limited experimental reports on oxides and nitrides. The error bars represent the range between the lowest and highest reported surface energy values as well as the variation based on crystallography orientations. As shown, metals typically exhibit higher surface energy compared to oxides and nitrides, and therefore, reported two-phase VAN systems can be categorized into two groups: (i) those comprising two materials with similar surface energy (two materials with low surface energy) and (ii) those with dissimilar surface energy (one material with low surface energy and the other with high surface energy). For example, the $BaTiO_3$–$CoFe_2O_4$ VAN system [33] belongs to the first group as both $BaTiO_3$ (1.24 J m^{-2}) [87] and $CoFe_2O4$ (1.48 J m^{-2}) [35] are oxides and exhibit comparable low surface energies. Conversely, the $BaTiO_3$–Au system represents the second group due to the distinct surface energies of $BaTiO_3$ (1.24 J m^{-2}) and Au (1.627 J m^{-2}) [85]. A detailed comparison of the growth mechanisms of these two groups will be discussed in later sections, aiding in understanding the role of surface energy in VAN structure formation.

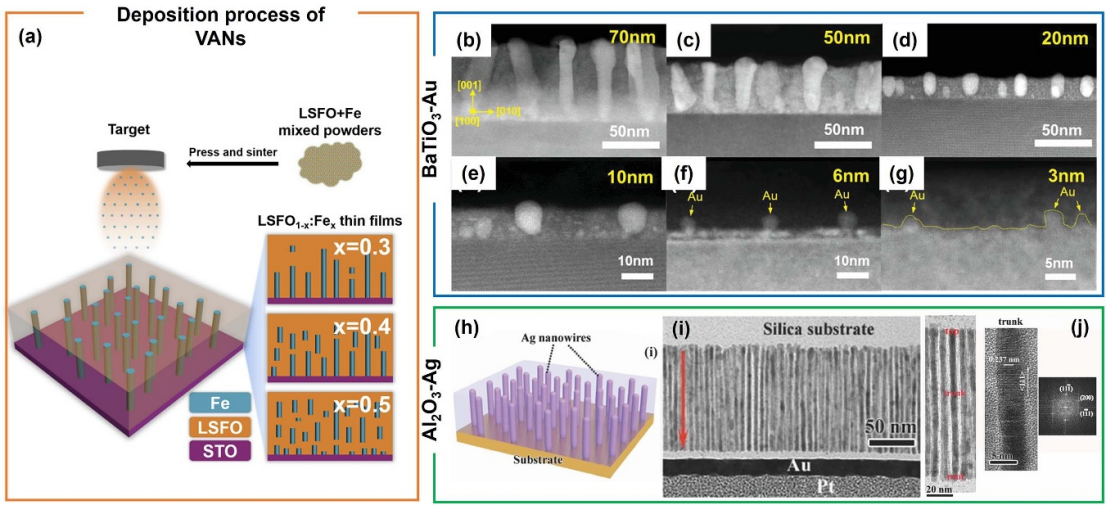

Figure 3. Growth mechanism of VANs combining two materials with dissimilar surface energy. (a) Full process of $La_{0.5}Sr_{0.5}FeO_3$–Fe VAN films involving target preparation, PLD set up, deposition and growth. Cross-section STEM images of BTO-Au thin films with different thicknesses: (b) 70 nm, (c) 50 nm, (d) 20 nm, (e) 10 nm, (f) 6 nm. [55] John Wiley & Sons. [© 2019 WILEY-VCH Verlag GmbH & Co. KGaA, Weinheim]. (g) 3 nm. (h) Schematic illustration of Al_2O_3–Ag nanocomposite thin film. (i) Cross-section and (j) high magnification cross-section images of Al_2O_3–Ag nanocomposite thin film. [90] John Wiley & Sons. [© 2017 WILEY-VCH Verlag GmbH & Co. KGaA, Weinheim].

3. PART II: Growth mechanisms of two-phase VANs

3.1. Combining two materials with dissimilar surface energy

3.1.1. Growth mechanisms

As new classes of VAN systems, oxide–metal and nitride–metal nanocomposite systems have attracted extensive research interests in recent years owing to their highly anisotropic microstructures and properties. These new anisotropic VAN systems grow as a new class of hybrid metamaterials with nanoscale tunability [27, 35, 63, 88, 89]. More interestingly, these new VAN systems can easily couple the novel functionalities from metals and nitrides with oxides, such as plasmonic properties, ferro- and ferrimagnetic properties, and catalytic properties [12, 63]. Metals typically exhibit higher surface energy than oxides and nitrides, making oxide (or nitride)-metal systems ideal for investigating the growth mechanism of VANs that combines two materials with dissimilar surface energies. The self-assembled VAN growth involves three main steps: target preparation, PLD setup, and deposition. As shown in figure 3(a) [53], the $La_{0.5}Sr_{0.5}FeO_3$(LSFO)-Fe target was prepared using a conventional ceramic sintering method. This process involves mixing LSFO and Fe powders in the appropriate atomic ratio, followed by pressing and sintering the mixture into a solid target. The PLD setup uses a high-energy laser to ablate the target surface, generating a plasma plume that contains the deposition species, which then forms a crystalline film on the substrate. During the deposition process, Fe undergoes an island growth mode, forming pillars, while LSFO follows a layer-by-layer growth mode, forming the matrix. These different growth behaviors of the two phases ultimately result in the formation of a typical VAN structure in LSFO-Fe films.

The detailed growth process can be visualized in the $BaTiO_3$ (BTO)-Au nanocomposite system [55–57], where BTO (with a low surface energy of 1.24 J/m^{2}[91]) and Au (with a high surface energy of 1.627 J/m^{2}[89]) were co-deposited. In this system, Au forms nano-sized pillars in the BTO matrix, resulting in a VAN structure. To explore the growth mechanism and visualize the nucleation and growth process, a systematic study of BTO-Au VAN thin films was conducted with precise control of film thickness from 3 to 70 nm (figures 3(b)–(g)) [55]. In the early stage of growth, Au adatoms tend to aggregate and nucleate into 3D islands to minimize the exposure of high-energy Au surfaces. These Au islands then serve as nucleation sites for subsequent Au deposition, leading to the formation of vertically aligned nanopillars within the BTO matrix. In addition to experimental demonstrations, a simulation study delved into the growth mechanism of oxide–metal VAN systems, focusing on Al_2O_3–Ag nanocomposite thin films where vertical Ag pillars form within an Al_2O_3 matrix by a self-assembled method (figures 3(h)–(j)) [90]. The adsorption energy of Ag on Al_2O_3 surface and Ag on Ag surface were calculated using density functional theory (DFT), considering Ag exposes its lowest energy planes of {111}. Results reveal that Ag adatoms preferentially grow on existing Ag surfaces rather than on Al_2O_3, due to higher adsorption energy, therefore promoting pillar formation. Both experimental and simulation findings indicate that a surface energy mismatch drives the formation of

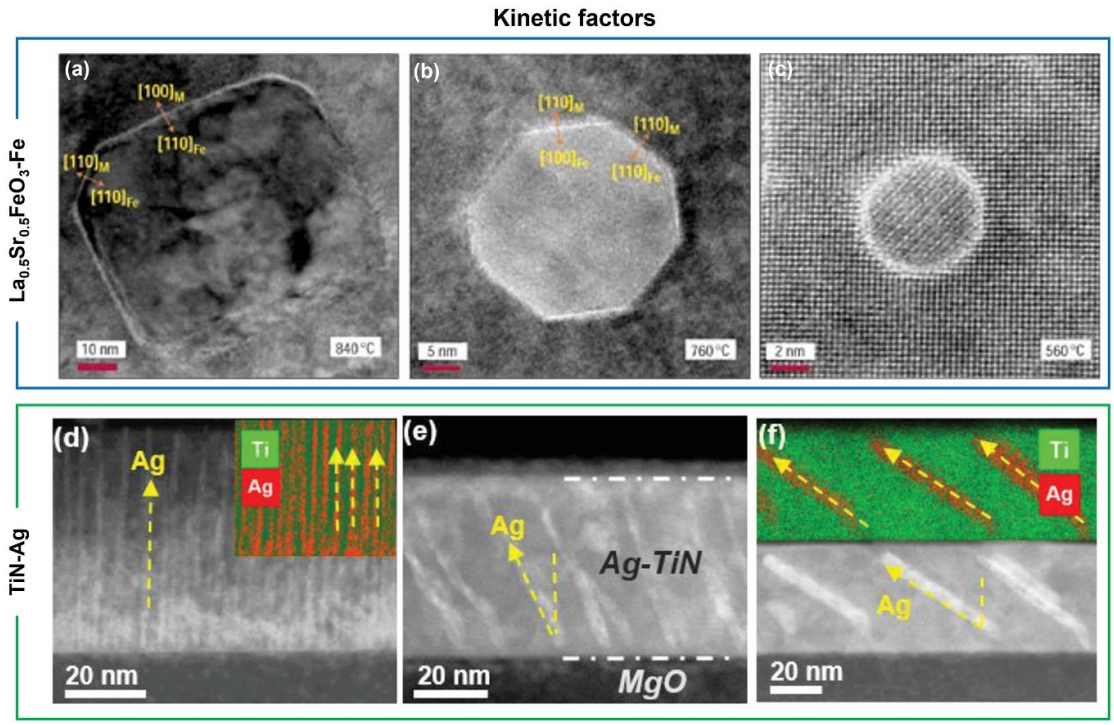

Figure 4. Influence of kinetic factors in VAN formation. Plan-view STEM images of Fe pillars in $La_{0.5}Sr_{0.5}FeO_3$–Fe nanocomposite thin film grown under (a) 840 °C, (b) 760 °C and (c) 560 °C. Cross-section STEM images of Ag pillars in TiN–Ag nanocomposite thin film with tiling angle of. Reproduced from [91], with permission from Springer Nature. (d) 0°, (e) 25° and (f) 50°. [62] John Wiley & Sons. [© 2018 WILEY-VCH Verlag GmbH & Co. KGaA, Weinheim].

vertically aligned nanostructures, with high-energy metals forming nanopillars within low-energy matrices through nucleation and aggregation processes.

3.1.2. Microstructure tunability

The detailed microstructure of VAN thin films significantly impacts their properties and functionalities. Therefore, many studies have concentrated on precisely tuning their microstructure to enhance performance. In oxide–metal or nitride–metal nanocomposites, the formation of VAN structure is mainly driven by the different surface energy and growth behavior between metallic phase and oxides or nitrides. However, the final microstructure is influenced by a combination of factors, not just surface energy. The following section explores several case studies that tunning VAN structure by changing growth kinetics, lattice strain and composition ratios.

Growth kinetic factors, such as temperature and deposition rate, are critical in determining the morphology of VANs in determining the rate of nucleation and growth, impacting the size, shape, and arrangement of the pillars. For example, varying the deposition temperature affects the mobility of adatoms, influencing their ability to form distinct crystallographic facets. Figures 4(a)–(c) shows the shape of Fe nanopillars can vary from circular to octagonal and square with changing growth temperatures [91]. At low deposition temperatures, a circular shape is preferred due to the limited adatom mobility, preventing the formation of distinct facets. At higher temperatures, Fe adatoms gain enough energy to form distinct facets, and the orientation of facets is determined by the surface energy of different facets. Since (110) is the lowest energy plane among all α-Fe crystallographic planes, they tend to dominate at higher temperatures and therefore form square-shaped nanowires. Another example is the tilting geometry observed in Ag–TiN nanocomposite thin films [62]. Under high deposition rates, Ag nanopillars grow vertically along the out-of-plane direction due to the limited diffusion time and length. Lower deposition rates allow Ag adatoms to search for more thermodynamically favorable sites. Therefore, the lowest energy plane of (111) tends to expose and finally cause tilted pillars.

Lattice strain can be exploited to fine-tune the ordering and orientation of nanopillars within oxide–metal or nitride–metal VANs. Figure 5 presents cross-section and plan-view scanning transmission electron microscopy (STEM) images of three nitride–metal nanocomposite thin films: TaN–Au on STO, TaN–Au on MgO, and TiN–Au on MgO [64, 92]. Notably, TaN–Au and TiN–Au composites exhibit successful VAN growth on these substrates, despite the considerable difference in lattice parameters between

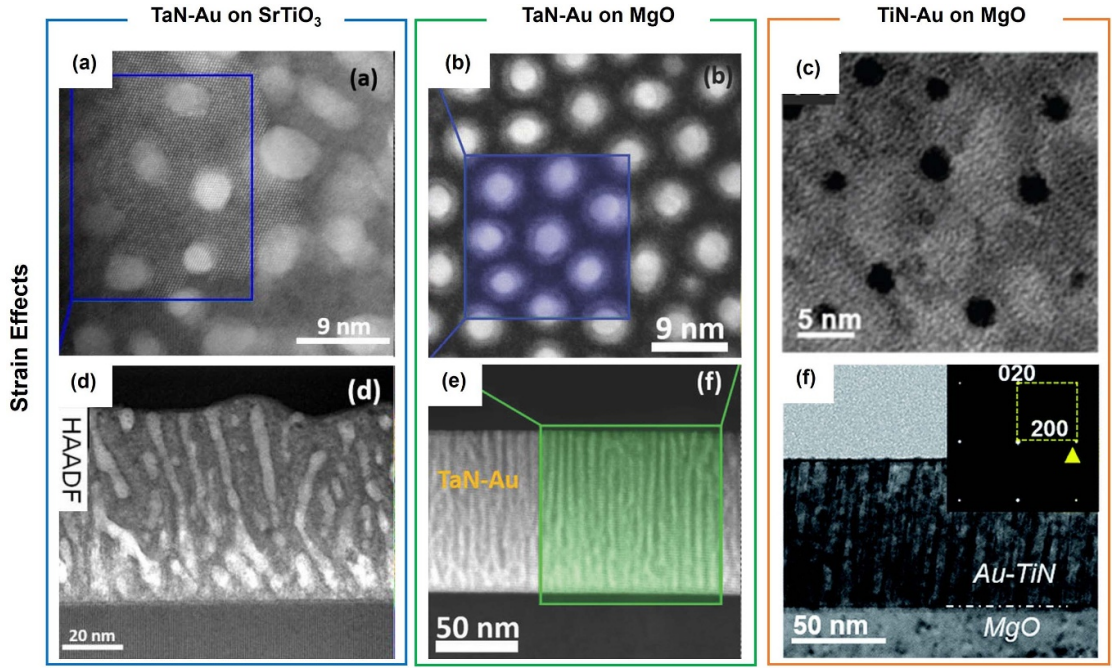

Figure 5. Influence of lattice strain in VAN formation. (a) Plan-view and (d) cross-section STEM images of TaN–Au nanocomposite film grown on $SrTiO_3$ substrate. (b) Plan-view and (e) cross-section STEM images of TaN–Au nanocomposite film grown on MgO substrate. Reproduced from [92]. CC BY 4.0. (c) Plan-view and (f) cross-section STEM images of TiN–Au nanocomposite film grown on MgO substrate. Reproduced with permission from [64]. CC BY-NC 3.0

STO ($a = 3.905$ Å) and MgO ($a = 4.21$ Å). Among these, the TaN–Au films grown on MgO substrates display the most ordered structures. Specifically, figures 5(b) and (e) reveal that the Au pillars in TaN–Au on MgO are arranged in a highly organized hexagonal pattern with a uniform in-plane distribution, which is not observed in the other two samples (TaN–Au on STO and TiN–Au on MgO). The highly ordered structure is attributed to the interplay of in-plane (between film and substrate) and out-of-plane (between pillars and matrix) strains. Specifically, the MgO substrate induces −3.68% strain to TaN and 3.55% strain to Au, resulting in a balanced state of compressive and tensile strains that enhance pillar ordering. Therefore, while surface energy is the primary driving force for the initial formation of oxide (or nitride)-metal VAN structures, lattice strain plays a critical role in shaping their final morphology and optimizing the VAN architecture. This opens up significant opportunities for strain engineering to tailor microstructure characteristics in nanocomposite films, providing a versatile approach for manipulating their functional properties.

The proportion of metal to oxide or nitride in a composite also affects the microstructure. Adjusting the composition ratio allows control over the distribution and density of metallic pillars within the composite structure, enabling tailored optimization of optical, electrical, or magnetic properties. For example, Wang *et al* carried out a series of syntheses on TiN–Au nanocomposite samples with varying Au densities, as illustrated in figures 6(a)–(c) [64]. The observed diameter of the Au pillars increases with higher Au ratios, subsequently influencing the optical properties of the TiN–Au thin film, such as the plasmonic resonance and dielectric constant. Another example is self-assembled LSMO-Au nanocomposite thin films with different Au ratios (figures 6(d)–(f)) [49]. In this case, while the diameter of Au pillars remained consistent across all samples, the density of the pillars increased with a higher concentration of Au. This investigation in modifying the composition ratio in oxide–metal and nitride–metal nanocomposite systems demonstrates their potential for customized microstructural adjustments to enhance functional properties.

3.2. Combining two materials with similar surface energy

Having explored the self-assembly processes in nanocomposite systems that combine materials with dissimilar surface energies, we now shift the focus to VANs that incorporate materials with similar surface energies. As previously mentioned, oxides generally exhibit relatively low surface energies, which tend to support a 2D layer-by-layer growth mode. This characteristic makes oxide–oxide nanocomposite systems an ideal platform for studying the driving forces behind VAN formation beyond surface energy considerations. In oxide–oxide nanocomposite films, the formation of vertical structures is primarily driven by two key factors: distinct crystalline structures and large lattice mismatch.

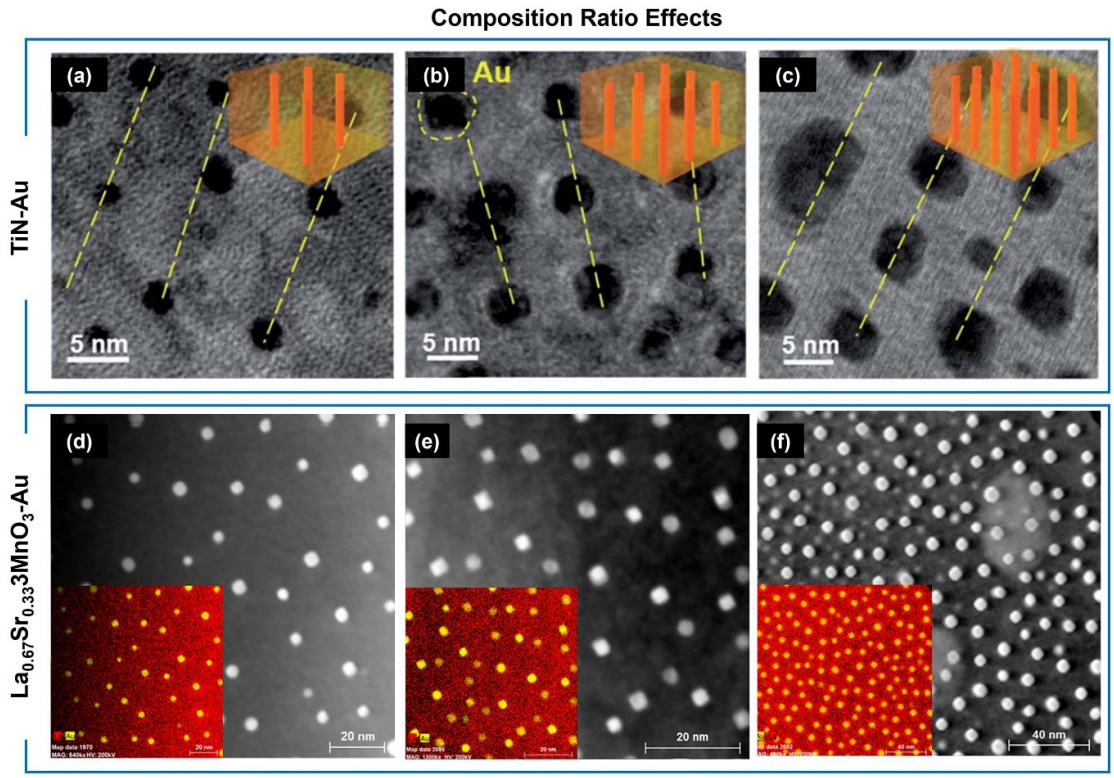

Figure 6. Influence of composition ratio in VAN formation. Plan-view STEM images of TiN–Au nanocomposite film with (a) low, (b) medium and (c) high Au ratios Plan-view STEM images of $La_{0.67}Sr_{0.33}MnO_3$–Au nanocomposite film with. Reproduced with permission from [64]. CC BY-NC 3.0 (d) low, (e) medium and (f) high Au pillar density. Reprinted with permission from [49]. Copyright (2021) American Chemical Society.

3.2.1. VAN systems with distinct crystalline structures

The perovskite–spinel system is one of the most studied systems in which two oxides can self-assemble into a VAN structure. A typical representative example of perovskite–spinel system is $BiFeO_3$(BFO)-$CoFe_2O_4$ (CFO) nanocomposite films [34, 93, 94]. By using one-step PLD process, CFO forms vertically aligned nanopillars embedded in BFO matrix on STO (001) substrate (figures 5(a)–(c)). This unique pillar-in-matrix structure is predominantly driven by the significant surface energy anisotropy of the two phases. Specifically, BFO has a perovskite structure and displays its lowest surface energy on the {001} planes, whereas CFO is a spinel oxide and exhibits the lowest surface energy on the {111} planes. This difference in surface energy anisotropy leads to distinct nucleation behaviors. CFO tends to expose its lowest energy {111} planes, following an island growth mode that favors the formation of nanopillars on (001) oriented substrates. Conversely, BFO prefers to expose its {001} planes and therefore are able to cover most of the substrate in a layer-by-layer growth mode. Interestingly, the roles of CFO and BFO are reversed when grown on (111) oriented substrates. On (111) oriented substrate, the wettability of CFO (111) planes surpasses that of BFO (001) planes, leading the formation of BFO nanopillars within a CFO matrix. This inversion of roles underscores the influence of substrate orientation on growth dynamics. Moreover, altering the composition ratio of BFO to CFO does not significantly impact the roles of the pillars and matrix, as well as the overall morphology of the VANs. This suggests that the BFO-CFO VANs have some degree of flexibility for tuning the composition ratio between the two phases.

The crystallographic surface energy anisotropy affects not only the roles of the constituent materials as either pillars or matrix, but also the resulted pillar shape. For example, CFO nanopillars exhibit different pillar shapes in BTO-CFO nanocomposites and BFO-CFO nanocomposites [33]. As shown in the plane-view images in figures 7(f) and (h), CFO phase forms cuboid-like pillars in a BFO matrix, while forms cylinder-like pillars in a BTO matrix. To understand these distinctive pillar features, it is essential to consider both the surface energy and lattice parameters of BFO and BTO. BTO has a higher surface energy (1.24 J m^{-2}) [87] compared to BFO (1 J m^{-2}) [95], and a larger lattice parameter (4.00 Å) than BFO (3.93 Å). With CFO having a lattice parameter of 8.26 Å (4.13 × 2 Å), the interface between BFO and CFO experiences greater strain than that between BTO and CFO. Consequently, the final shape of the CFO nanopillars is largely influenced by the interplay between surface energy and strain energy. In the BTO-CFO system, where the strain energy at the interface is minor compared to the relatively high surface energy of

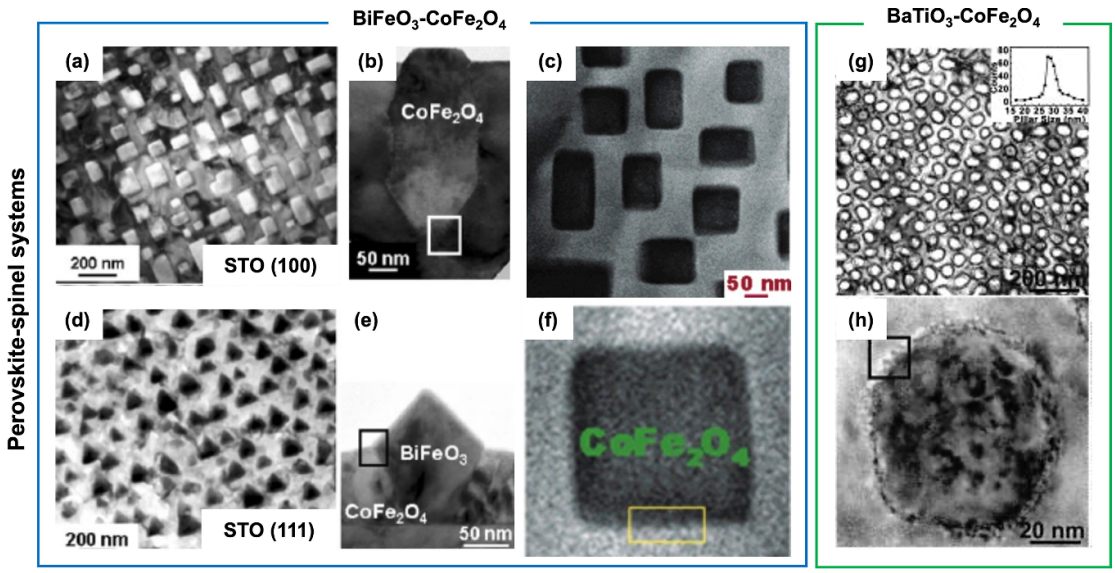

Figure 7. Self-assembled perovskite–spinel nanocomposite systems. (a) Plan-view and (b) cross-section STEM images of $BiFeO_3$–$CoFe_2O_4$ nanocomposite film grown on $SrTiO_3$ (100) substrate. (d) Plan-view and (e) cross-section STEM images of $BiFeO_3$–$CoFe_2O_4$ nanocomposite film grown on $SrTiO_3$ (111) substrate. [34] John Wiley & Sons. [Copyright © 2006 WILEY-VCH Verlag GmbH & Co. KGaA, Weinheim]. (c) Low-magnification and (f) high-magnification of plan view images of $BiFeO_3$–$CoFe_2O_4$ nanocomposite film. Reprinted with permission from [35]. Copyright (2006) American Chemical Society. (g) Low-magnification and (h) high-magnification of plan view images of $BaTiO_3$–$CoFe_2O_4$ nanocomposite film. Reprinted from [33], with the permission of AIP Publishing.

CFO, the CFO phase tends to form cylinder shapes to minimize the exposure of the CFO surface, reducing the system's overall energy. Conversely, in the BFO-CFO system, the significant strain energy at the interface becomes a critical factor, leading to the formation of cuboid CFO pillars to minimize the interface area, thereby reducing the strain energy.

In addition to perovskite–spinel systems, perovskite–wurtzite systems have also been successfully developed into VANs [96, 97] through self-assembly processes. An illustrative example is $La_{0.7}Sr_{0.3}MnO_3$(LSMO)-ZnO nanocomposite thin films, where ZnO nanoplates are vertically aligned within a LSMO matrix on STO substrates [96]. Due to the large difference in the crystal symmetry between wurtzite ZnO and perovskite STO, ZnO phase has a tendency to grow in 3D island mode during the nucleation and growth process. To minimize the in-plane strain across from the ZnO-STO interface, ZnO forms rectangle nanoplates that orient in two distinct configurations, as illustrated in figure 8. The phi (φ)-scan x-ray diffraction (XRD) results of ZnO (1010) planes shows four-fold symmetry, confirming a 90° in-plane rotation of two possible matching orientations, labeled as states A and B. This structural arrangement results in the unique nanomaze architecture observed in the LSMO-ZnO nanocomposites. Furthermore, the variability in the composition ratio of LSMO:ZnO was reported to range from 0.7:0.3–0.3:0.7, suggesting extensive flexibility in tuning the composition of these systems.

3.2.2. VAN systems with large lattice mismatch

A significant lattice mismatch between the two phases in a composite can also lead to the formation of a VAN structure, especially when the two phases share similar crystallographic structures but differ in lattice parameters. When one phase has a lattice parameter significantly different from that of the substrate, it tends to nucleate as 3D islands to minimize the strain energy. Another phase is selected with relatively low strain energy and favoring 2D layer-by-layer growth and therefore the combinational growth of 2D and 3D modes results in a VAN formation. An example is $SrTiO_3$–MgO (STO-MgO) VAN thin film grown on STO substrate [98]. STO has a perovskite structure with a lattice parameter of approximately 3.905 Å, while MgO exhibits a rock salt structure with a lattice parameter of approximately 4.21 Å. Both have cubic structures with {100} plane being the lowest energy plane and therefore STO-MgO nanocomposite system is a good case to minimize the influence of structural mismatch. As shown in the microstructure images in figures 9(a) and (b), MgO forms nanopillars vertically embedded in the STO matrix. This VAN formation is primarily driven by the large lattice mismatch between MgO and the STO substrate. This mismatch typically encourages MgO to form islands to minimize the high interfacial energy resulting from the mismatch. Furthermore, the STO matrix experiences approximately 1.5% strain due to lattice coupling with the out-of-plane MgO pillars, thereby achieving strain-induced ferroelectricity using this nanocomposite approach.

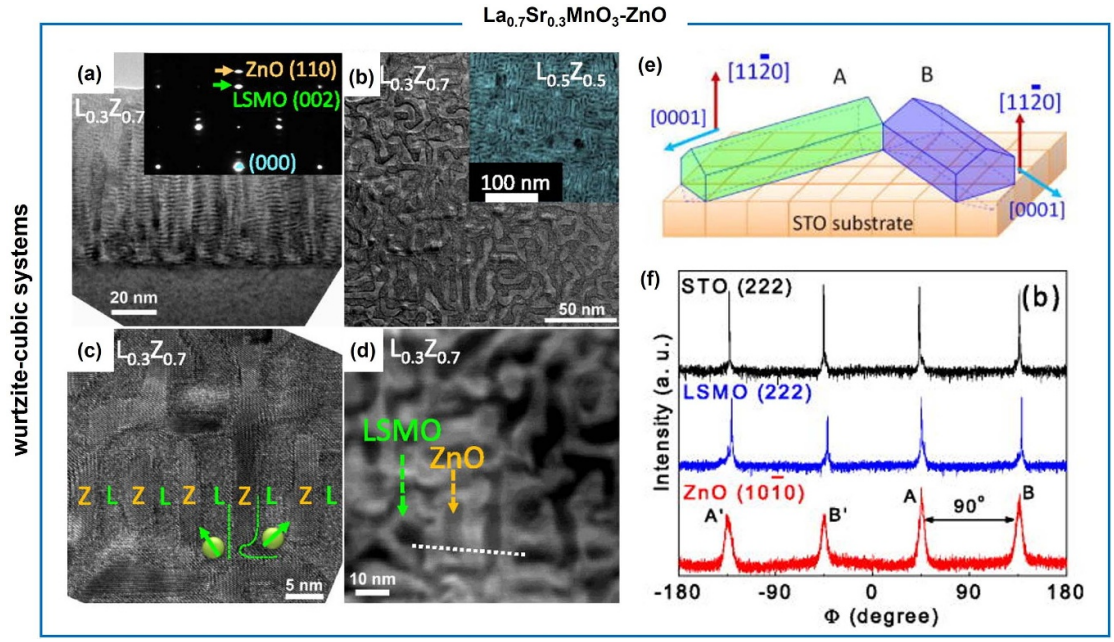

Figure 8. Self-assembled wurtzite-cubic nanocomposite systems. (a) Low-magnification and (c) high-resolution cross-section STEM images of $La_{0.3}Sr_{0.7}MnO_3$–ZnO nanocomposite film with a $La_{0.3}Sr_{0.7}MnO_3$:ZnO ratio of 0.3:0.7. (b) Low-magnification and (d) high resolution plan-view STEM images of $La_{0.3}Sr_{0.7}MnO_3$–ZnO nanocomposite film. (e) Schematic illustration of the growth orientation of the ZnO phase. (f) Phi-scan x-ray diffraction of $La_{0.3}Sr_{0.7}MnO_3$–ZnO nanocomposite film. Reprinted from [96], with the permission of AIP Publishing.

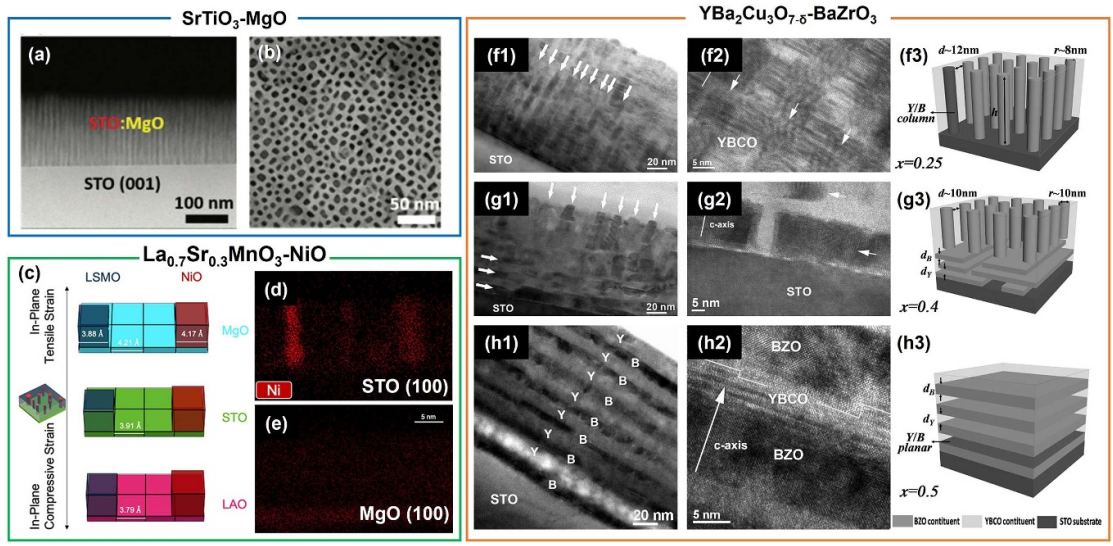

Figure 9. Oxide–oxide nanocomposite films driven by lattice mismatch. (a) Cross-section and (b) plan-view of STEM images of $SrTiO_3$–MgO nanocomposite film. Reproduced from [98] with permission from the Royal Society of Chemistry. (c) Schematic illustration of the lattice matching in $La_{0.7}Sr_{0.3}MnO_3$–NiO nanocomposites. Cross-section STEM-EDS map showing Ni distribution in $La_{0.7}Sr_{0.3}MnO_3$–NiO nanocomposites grown on $SrTiO_3$ (100) and MgO (100) substrates. Cross-section of STEM images of $YBa_2Cu_3O_{7-\delta}$–$BaZrO_3$ nanocomposite film with a $BaZrO_3$ concentration of. Reproduced from [99]. CC BY 4.0. (f) 0.25, (g) 0.4, and (h) 0.5. [100] John Wiley & Sons. [© 2014 WILEY-VCH Verlag GmbH & Co. KGaA, Weinheim].

Controlling the strain states of two phases in oxide–oxide VANs is crucial for achieving the desired growth quality and film morphology. One specific example is the growth of LSMO-NiO nanocomposite film on STO substrate compared with MgO substrate [99]. On a STO substrate, LSMO and NiO form a typical VAN structure where NiO pillars are clearly embedded within the LSMO matrix, as shown in figure 9(d). The formation of NiO pillars is primarily driven by the significant lattice mismatch between NiO ($a = 4.17$ Å) and the STO substrate ($a = 3.905$ Å). However, changing the substrate material to a more closely matched MgO ($a = 4.21$ Å) results in a disappearance of NiO pillars, where the LSMO-NiO thin film no longer exhibits clear phase separation (figure 9(e)). This loss of VAN morphology suggests that the

LSMO-NiO system is sensitive to the in-plain strain states. Another representative example is the study of $YBa_2Cu_3O_{7-\delta}$–$BaZrO_3$ (YBCO-BZO) films with different composition ratios (figure 9(f)–(h)) [100]. With the BZO ratio below 0.4, BZO forms vertical pillars embedded within the YBCO, driven by the significant lattice mismatch with the STO substrate. As the BZO ratio increases, a microstructure transition has been observed from a vertical columnar structure to a horizontal multilayered structure. To understand the mechanism behind this microstructure transition, an energetic analysis of interfacial energy for both columnar and planar structures was conducted. BZO, having a larger lattice parameter and Young's modulus than YBCO, induces significant strain on the YBCO matrix as its ratio increases. This strain continues to build up with increasing BZO ratio. In the horizontal case, the YBCO phase is still strained, but the strain does not build up with increasing BZO amount. This is because partial strain can be relaxed through misfit dislocation. Eventually, at a certain point ($x = 0.4$), forming a multilayer structure becomes energetically more favorable due to the large strain induced by vertical YBCO-BZO interfaces. These examples illustrate that, for the VAN system driven by lattice mismatch, changes in substrate material and composition ratios can lead to significant alterations in microstructure, highlighting the sensitivity of these VAN systems to those variations. Above all, such fine tuning of film morphologies in oxide–oxide VAN systems based on substrate orientation selection, phase composition, and growth parameters is all traced back to their very close surface energy between the two oxide phases, which is very different from the oxide–metal and nitride–metal cases with very dissimilar surface energy.

4. PART III: beyond two-phase VANs

Beyond the reported two-phase VAN systems, recent studies on multi-phase nanocomposite designs have demonstrated their great potential in enhancing structure complexity, property tunability and functionality coupling. Taking advantages of the self-assembled VANs, more complex nanostructures can be formed by adding a third phase or stacking VAN layers. However, incorporating multiple materials into self-assembled VAN-related structures has been challenging due to materials constraints and deposition complexities arising from differing growth kinetics. Careful control of the surface energy of each component is crucial for forming and engineering complex VAN structures. This approach opens up new avenues for innovation and exploration of nanostructures with tailored properties and functionalities for diverse applications in nanotechnology, electronics, and photonics. In this section, we review several multi-phase VAN systems and discuss the role of surface energy in these systems.

4.1. VANs with core–shell nanopillars

One novel structure within complex VAN nanostructures is core–shell nanopillars, where distinct compositions form pillars with a core material surrounded by a shell material. An illustrative example of this core–shell structure can be found in BTO-AuCuCoNi systems, where alloy nanopillars, consisting of four elements (i.e. Au, Cu, Co, and Ni) were vertically aligned within a BTO matrix, as shown in schematic and cross-sectional images in figure 10(a) [101]. Here, the CoNi alloy forms the core, surrounded by an inner Cu shell and an outer Au shell. Similar to two-phase oxide–metal VAN systems, the metallic phases follow a Volmer–Weber 3D island growth mode and form nanopillars due to their high surface energy, while the BTO matrix undergoes layer-by-layer growth to form the matrix. The formation of core–shell nanopillars is driven by the disparity in surface energy. Specifically, among the four metals, Co possesses the highest surface energy, followed by Ni, Cu, and Au. Consequently, during nucleation and growth, CoNi tends to form the core to minimize exposure, followed by the Cu and Au shells, due to their lower surface energy relative to CoNi. These BTO-alloy nanocomposites combine magnetic Co and Ni with plasmonic Cu and Au in a vertically aligned configuration, thereby exhibiting highly anisotropic optical and magnetic responses, as well as demonstrating magneto-optical coupling effect.

Surface energy not only plays an important role in the formation of core–shell structures but also shapes their configuration. In TiN–Au–$CoFe_2$ nanocomposite films (figures 10(b) and (c) [59]), three distinct configurations of Au–$CoFe_2$ nanopillars are observed, each characterized by unique surface facet exposures and growth orientations. Type I nanopillars feature inner Au (002) cores and outer $CoFe_2$ (110) shells, while type II has inner $CoFe_2$ (002) cores and outer Au (002) shells. Type III nanopillars exhibit half-shaped Au (002) shells encircling $CoFe_2$ (110) cores. These structural variations are primarily attributed to a combinational effect of surface energy and lattice strain. Specifically, $CoFe_2$ nucleates as 3D islands on both (110) and (002) facets simultaneously due to their comparable high surface energy. When $CoFe_2$ nucleates with a (002) orientation, Au (002) experiences a significant lattice mismatch and therefore grows around $CoFe_2$ to form an outer shell (type II) to reduce the strain energy. Conversely, if $CoFe_2$ nucleates with (011) orientation, if $CoFe_2$ nucleates with a (011) orientation, Au can either form the inner core (type I) or the outer half shell (type III) as Au (002) aligns well with $CoFe_2$ (110).

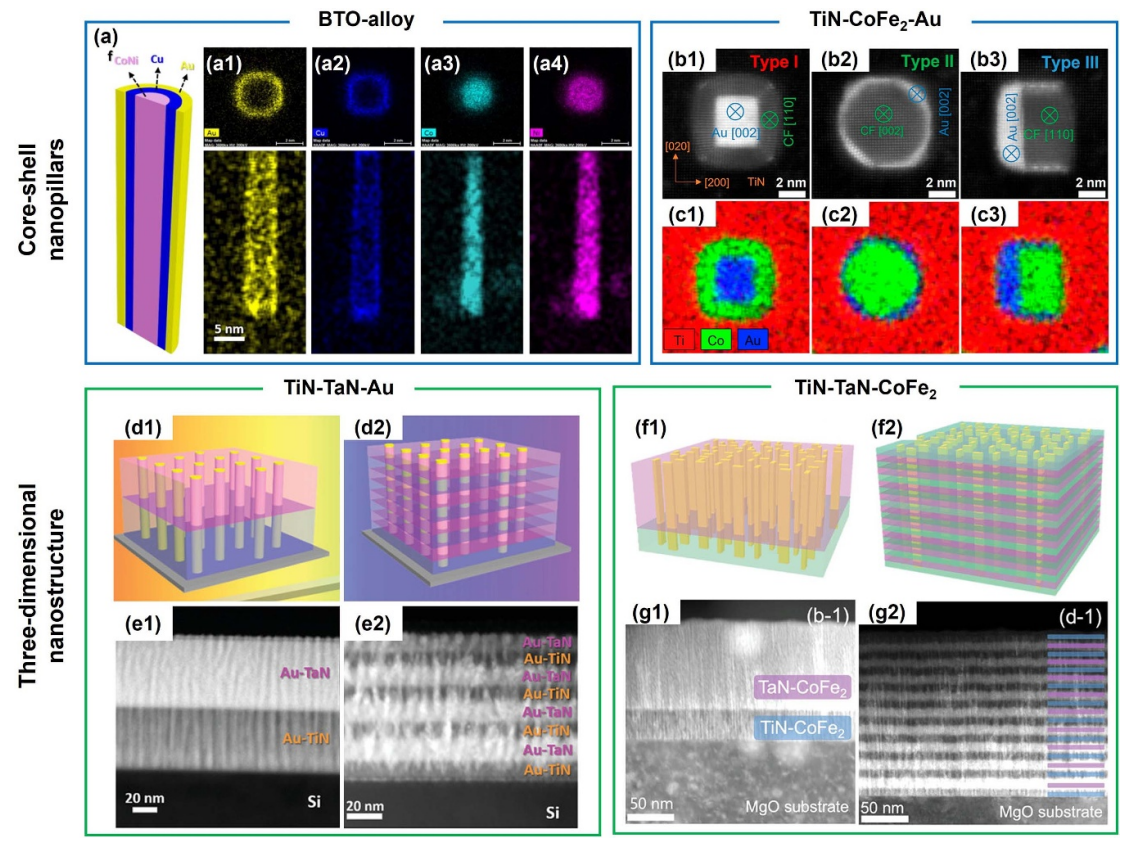

Figure 10. Beyond two-phase nanocomposites. (a) Schematic illustration of alloy pillars in $BaTiO_3$-alloy nanocomposite films with (a1–a4) EDS mapping of Au, Cu, Co, Ni. Reprinted from [101], Copyright (2021), with permission from Elsevier. (b) Plan-view STEM images of (b1) Type I, (b2) Type II and (b3) Type III of the core–shell pillars in TiN–$CoFe_2$–Au VANs. (c) Plan-view EDS mappings of (c1) Type I, (c2) Type II and (c3) Type III of the core–shell pillars in TiN-$CoFe_2$–Au VANs. Reprinted with permission from [59]. Copyright (2023) American Chemical Society. (d) Schematic illustration of (d1) 2-layer and (d2) 8-layer TiN–TaN–Au nanocomposite films. (e) Cross-section STEM images of (e1) 2-layer and (e2) 8-layer TiN–TaN–Au nanocomposite films. [102] John Wiley & Sons. [© 2020 WILEY-VCH Verlag GmbH & Co. KGaA, Weinheim]. (f) Schematic illustration of (f1) 2-layer and (f2) 19-layer TiN–TaN–$CoFe_2$ nanocomposite films. (g) Cross-section STEM images of (g1) 2-layer and (g2) 19-layer TiN–TaN–$CoFe_2$ nanocomposite films. Reproduced from [58]. CC BY 4.0.

Overall, the miscibility of the materials involved in the deposition process is a key factor in determining whether a core–shell or alloy structure will form. When the materials are miscible, they tend to mix at the atomic level during growth, leading to the formation of homogeneous alloy pillars. For instance, CoNi and CoPt are examples of miscible alloys, which results in uniform alloy nanopillars in systems like CoNi–$SrTiO_3$ and CoPt–$SrTiO_3$ [103, 104], rather than distinct core–shell structures, The relative surface energies of the different metals significantly influence the detailed structure of core–shell pillars, such as which material forms the core and which forms the shell. Typically, materials with higher surface energy tend to nucleate first and form the inner core to minimize the exposed surface area. In contrast, materials with lower surface energy tend to form the outer shell. Deposition parameters also have a substantial influence on the final morphology. For instance, despite that Au and Fe are typically thermodynamically immiscible, increasing the deposition rate during the process can result in a well-mixed alloy pillar [51]. This occurs primarily because the limited diffusion under high deposition laser frequency, prevents the materials from phase separation as core–shell structures.

4.2. VANs with three-dimensional nanostructure

Combining multilayer structures with VAN structures offers a compelling approach to fabricating complex 3D microstructures. In this approach, the pillars formed in the lower layers act as nucleation sites to facilitate the nucleation process of subsequent layers, enabling the controlled deposition and alignment of materials in the upper layers. By carefully selecting materials with compatible surface energies and growth behaviors, sequential deposition of two or more VAN nanolayers can form complex 3D nanostructure. Figures 10(d) and (e) show a series of complex 3D nanocomposite films which incorporate ultrafine gold (Au) nanopillars and alternating TiN and TaN nanolayers [102]. Such a 3D structure was achieved by a continuous growth of Au nanopillars, primarily driven by preferential Au nucleation on existing Au seeds.

One of the major advantages of the innovative 3D nanostructure design is it offers large freedom in manipulating light-matter interactions at the nanoscale, particularly in controlling their hyperbolic behavior. Hyperbolic behavior refers to highly anisotropic optical properties where the permittivity has opposite signs along different directions. Nanopilallrs or nanowires structures typically demonstrate Type I hyperbolic dispersion, where out-of-plane permittivity is negative and in-plane permittivity is positive. Examples include BTO-Au VANs LSMO-Au VANs [49, 57]. Multilayer structures often exhibit Type II hyperbolic dispersion, characterized by negative in-plane and positive out-of-plane permittivity values, as seen in TiN/MgO and TiN/AlScN multilayers [66, 105]. Precise control over the combination of VAN and multilayer structures allows for the manipulation of optical properties in 3D nanocomposites, and can even achieve a transition between Type I and Type II dispersions. For example, a 3D nanostructure was designed by alternating deposition TiN/$CoFe_2$ nanolayers and TaN/$CoFe_2$ nanolayers (figures 10(f) and (g)) [58]. By increasing the number of stacking layers from 2 to 19, a hyperbolic transition from type II to type was observed.

5. Summary and outlook

5.1. Summary

In this review, the growth mechanisms of various VAN systems have been systematically discussed and compared, with a particular focus on the roles that surface energy play in VAN formation. Overall, there are three main driving forces for the formation of VAN structures:

(i) Surface Energy: Materials with high surface energy tend to form vertical pillars through island growth, while those with low surface energy prefer a two-dimensional, layer-by-layer growth mode. Alterations in growth parameters, strain, or composition ratio of the thin film do not necessarily impact the overall VAN formation, although precise control of these and other factors is crucial for forming highly ordered nanopillars. This is particularly obvious in the oxide–metal and nitride–metal systems with very dissimilar surface energy, and thus the high surface energy phase will form the pillars and the low surface energy phase will grow as the matrix. The surface energy also controls the tilting and shape of the nanopillars and thus plays a critical role in controlling the final resulted VAN morphologies. Such surface energy effects become less dominant in the oxide–oxide VANs with similar surface energy. In these cases, other factors such as the lattice strain, substrate selections and orientations, and growth parameters play more effective roles in VAN morphology tuning.

(ii) Crystal Structure: The distinct crystal structures of the materials enable differential growth modes on a substrate. The wetting ability, which is critical for defining the roles of pillars and matrix within the composite, is strongly influenced by crystal symmetry and growth orientation. Notably, reversing the substrate orientation can lead to a switch in the roles of the pillars and matrix, significantly affecting the final morphology in conjunction with surface energy and lattice strain. As previously discussed, in oxide–metal and nitride–metal cases, such crystal structure effects are less studied and also considered to be less effective considering the dominant surface energy effects. In oxide–oxide cases, such crystal structure effects are found to be very effective in tuning the overall phase morphologies evidenced by the versatile morphologies demonstrated and effective tuning in VAN systems grown on various substrates or substrates with different orientations.

(iii) Lattice Mismatch: In systems where materials have similar surface energy and crystal structure, lattice mismatch becomes a critical factor. A significant mismatch can induce substantial strain energy at the interfaces, promoting an island growth mode. Such systems generally require a small ratio of pillar material to matrix and a reasonable lattice mismatch. Alterations in either the composition ratio or strain can lead to the loss of the VAN structure. Again this is a dominant factor in many of the oxide–oxide VANs considering the similar surface energy and crystal structures. The lattice mismatch will introduce significant strain in vertically coupled interfaces and thus impacts on their resulted physical properties out-of-plane.

Among the three major factors, surface energy is considered the most powerful factor in forming VAN structure. Figure 2 provides a guideline for materials selections for designing VAN systems based on surface energy and lattice parameter. Selecting a combination of high surface energy metals with low surface energy oxides or nitrides significantly increases the likelihood of achieving a VAN structure. Such VAN systems typically are robust regardless of the changes in strain or other kinetic parameters, thereby offering considerable flexible tunability. There are few exceptions, such as VO_2–Au and VO_2–Pt, LiNbO3–Au, and BNMO-Au [6, 106–108], where the metal phase forms nanoparticles regardless of the growth conditions. In these oxide–metal nanocomposite systems, the matrix oxides are mostly layered oxide structures with very

strong preferred 2D-layered growth mode. Thus, the continuous growth of metallic pillars becomes challenging in these cases. Except in those cases, most of the oxide–metal demonstrations are shown to be VANs.

On the other hand, when combining two low surface energy materials, such as oxide–oxide or nitride–oxide systems, careful design and selections of lattice mismatch/strain and the optimization of deposition conditions are necessary to achieve the desired VAN structures. As abovementioned, these systems are more sensitive to the change in lattice mismatch and substrate orientations and thus completely different two-phase morphologies could be resulted. The tuning of growth parameters is also quite effective in morphology tuning and property optimizations.

5.2. Outlook

Looking forward, there are enormous amount of new VAN systems to be explored. With the presented generalized materials design guidelines, we are proposing the following research directions.

First, with the current understanding of the surface energy role in forming VAN structures, using templated methods or seed layers is an effective approach for facilitating and optimizing the growth of VAN films. Initially, a thin seed layer featuring nanosized structures is deposited on the substrate. This seed layer significantly promotes the nucleation of the nanopillars, guiding them to the desired orientation and phase [24]. This approach helps reduce strain and align the crystallographic orientation of the subsequent layers, thereby optimizing the overall microstructure of the VAN films. The seeding approaches can be used to grow other VAN systems that are challenging to achieve directly, for example, the successful demonstration of BTO-ZnO growth using BTO-Au as a seed layer [109].

Second, the research on VAN thin films has focused on oxide–oxide, metal–oxide, and nitride–metal systems, while there are very limited successes in nitride–oxide combinations [65, 110] and other systems. This gap presents a significant research opportunity, especially considering the unique plasmonic properties of transition-metal nitrides and the diverse functionalities of oxides. Similar to oxide–oxide combinations, coupling nitrides with oxides involves combining two materials with comparably low surface energies. Therefore, investigating nitride–oxide nanocomposites on variously oriented substrates or carefully selecting materials with significant lattice mismatches could facilitate phase segregation and pillar formation, thereby expanding the understanding and potential applications of the nitride–oxide systems.

Third, a comprehensive database detailing the surface energy of various materials is essential for the research and development of VANs, particularly for understanding and predicting their formation. While the surface energy of metals is well-researched and documented, similar extensive studies are lacking for oxides and nitrides. For example, data on metals such as Au are quite precise; experimental studies by Tyson and Boer have reported the surface energy of Au to be approximately 1.506 J m^{-2} and 1.500 J m^{-2}, respectively [111, 112]. Additionally, computational studies by Vitos using DFT estimated the surface energy of Au (100) at about 1.627 J m^{-2}[89]. A complete database of surface energy values for oxides and nitrides, established through both experimental and computational studies, could significantly aid in the design and synthesis of new VAN materials. Such a resource would not only support ongoing research but also improve the development of customized nanocomposites and enable more accurate predictions of material behavior in various applications.

Fourth, while VANs have been extensively investigated experimentally with various material combinations, there is a need for a deeper understanding of the thermodynamics and kinetics of VAN growth through theoretical calculations. For example, a DFT-based kinetic Monte Carlo simulation model has been used to describe the growth of CeO_2–Au VANs [113]. Moving forward, these computational investigations could be applied to explore other material combinations and complex structures, such as core–shell nanopillars and 3D nanostructures. Expanding the scope of material systems can further enhance our understanding of growth mechanisms, thereby facilitating the exploration and development of advanced VANs.

Fifth, there are very limited demonstrations in VAN-based devices [114–117] and thus more device demonstrations could bring the power of VANs into practical applications. With their tunable physical properties and unique multifunctionalities, VANs hold promise for applications in electronics and optical devices. Considering the good epitaxial quality required by VANs, one significant challenge lies in the integration of VANs onto Si or flexible substrates (i.e. mica). Employing buffer layers such as STO/TiN has shown promise in maintaining the desired epitaxial quality and vertical nanostructure on Si substrates [118, 119]. Another promising approach is transferring free-standing VAN layers onto Si wafers. This method involves peeling off the free-standing VAN layer from a conventional substrate, such as STO or MgO, with the assistance of a water-soluble buffer layer [36, 120, 121]. These demonstrations could also allow the integration of plasmonic, magnetic, ferroelectric, and multiferroic properties of the freestanding VANs on existing device platforms.

Data availability statement

All data that support the findings of this study are included within the article (and any supplementary files).

Acknowledgments

This work was supported by the U.S. National Science Foundation DMR-2016453 (nitride-based VAN thin films) and DMREF-2323752 (VAN transfer and device applications). The oxide–metal based VAN work was supported by the U.S. Department of Energy, Office of Science, Basic Energy Sciences with Award No. DE-SC0020077.

ORCID iDs

Jiawei Song https://orcid.org/0000-0003-4013-1200
Haiyan Wang https://orcid.org/0000-0002-7397-1209

References

[1] Au K, Gao X S, Wang J, Bao Z Y, Liu J M and Dai J Y 2013 Enhanced resistive switching effect in Ag nanoparticle embedded $BaTiO_3$ thin films *J. Appl. Phys.* **114** 027019
[2] Hao Q *et al* 2018 VO_2/TiN plasmonic thermochromic smart coatings for room-temperature applications *Adv. Mater.* **30** 1–5
[3] Wang Z, Kortge D, He Z, Song J, Zhu J, Lee C, Wang H and Bermel P 2022 Selective emitter materials and designs for high-temperature thermophotovoltaic applications *Solar Energy Mater. Solar Cells* **238** 111554
[4] Liu H J, Liang W I, Chu Y H, Zheng H and Ramesh R 2014 Self-assembled vertical heteroepitaxial nanostructures: from growth to functionalities *MRS Commun.* **4** 31–44
[5] Misra S, Li L, Jian J, Huang J, Wang X, Zemlyanov D, Jang J-W, Ribeiro F H and Wang H 2018 Tailorable Au nanoparticles embedded in epitaxial TiO_2 thin films for tunable optical properties *ACS Appl. Mater. Interfaces* **10** 32895–902
[6] Jian J *et al* 2019 Broad range tuning of phase transition property in VO_2 through metal-ceramic nanocomposite design *Adv. Funct. Mater.* **29** 1903690
[7] Roy Chowdhury P, Khot K, Song J, He Z, Kortge D, Han Z, Bermel P, Wang H and Ruan X 2024 Machine learning designed and experimentally confirmed enhanced reflectance in aperiodic multilayer structures *Adv. Opt. Mater.* **12** 2300610
[8] Song J *et al* 2024 Design of all-oxide multilayers with high-temperature stability toward future thermophotovoltaic applications *Adv. Mater. Interfaces* **11** 2300733
[9] Zhang W, Chen A, Bi Z, Jia Q, MacManus-Driscoll J L and Wang H 2014 Interfacial coupling in heteroepitaxial vertically aligned nanocomposite thin films: from lateral to vertical control *Curr. Opin. Solid State Mater. Sci.* **18** 6–18
[10] MacManus-Driscoll J L, Zerrer P, Wang H, Yang H, Yoon J, Fouchet A, Yu R, Blamire M G and Jia Q 2008 Strain control and spontaneous phase ordering in vertical nanocomposite heteroepitaxial thin films *Nat. Mater.* **7** 314–20
[11] Sun X, Huang J, Jian J, Fan M, Wang H, Li Q, Mac Manus-Driscoll J L, Lu P, Zhang X and Wang H 2018 Three-dimensional strain engineering in epitaxial vertically aligned nanocomposite thin films with tunable magnetotransport properties *Mater. Horiz.* **5** 536–44
[12] Misra S and Wang H 2021 Review on the growth, properties and applications of self-assembled oxide–metal vertically aligned nanocomposite thin films—current and future perspectives *Mater. Horiz.* **8** 869–84
[13] Wang X *et al* 2020 Large-scale plasmonic hybrid framework with built-in nanohole array as multifunctional optical sensing platforms *Small* **16** 1–10
[14] Lin J-F, Bird J P, Rotkina L and Bennett P A 2003 Classical and quantum transport in focused-ion-beam-deposited Pt nanointerconnects *Appl. Phys. Lett.* **82** 802–4
[15] Zhao Z J *et al* 2017 Three-dimensional plasmonic Ag/TiO_2 nanocomposite architectures on flexible substrates for visible-light photocatalytic activity *Sci. Rep.* **7** 8915
[16] Burckel D B, Resnick P J, Finnegan P S, Sinclair M B and Davids P S 2015 Micrometer-scale fabrication of complex three dimensional lattice + basis structures in silicon *Opt. Mater. Express* **5** 2231
[17] Liu N, Guo H, Fu L, Kaiser S, Schweizer H and Giessen H 2008 Three-dimensional photonic metamaterials at optical frequencies *Nat. Mater.* **7** 31–37
[18] Kamakura R, Murai S, Ishii S, Nagao T, Fujita K and Tanaka K 2017 Plasmonic-photonic hybrid modes excited on a titanium nitride nanoparticle array in the visible region *ACS Photonics* **4** 815–22
[19] Li W, Guler U, Kinsey N, Naik G V, Boltasseva A, Guan J, Shalaev V M and Kildishev A V 2014 Refractory plasmonics with titanium nitride: broadband *Adv. Mater.* **26** 7959–65
[20] Pendry J B, Schurig D and Smith D R 2006 Controlling electromagnetic fields *Science* **312** 1780–2
[21] Fang Z, Wang Y, Peng X, Liu X and Zhen C 2003 Structural and optical properties of ZnO films grown on the AAO templates *Mater. Lett.* **57** 4187–90
[22] Chahrour K M, Ahmed N M, Hashim M R, Elfadill N G, Qaeed M A and Bououdina M 2014 Preparation of thin hexagonal highly-ordered anodic aluminum oxide (AAO) template onto silicon substrate and growth ZnO nanorod arrays by electrodeposition *Superlattices Microstruct.* **76** 197–204
[23] Wang J and Lin Z 2008 Freestanding TiO_2 nanotube arrays with ultrahigh aspect ratio via electrochemical anodization *Chem. Mater.* **20** 1257–61
[24] Hu Z, Lu J, Dou H, Shen J, Barnard J P, Liu J, Zhang X and Wang H 2024 Template-assisted growth of Co-$BaTiO_3$ vertically aligned nanocomposite thin films with strong magneto-optical coupling effect *Nano Res.* **17** 3130–8
[25] Chahrour K M, Ahmed N M, Hashim M R, Elfadill N G and Qaeed M A 2014 Controllable fabrication of highly ordered thin AAO template on Si substrate for electrodeposition of nanostructures *Appl. Phys.* A **116** 1389–93
[26] Wen L, Xu R, Mi Y and Lei Y 2017 Multiple nanostructures based on anodized aluminium oxide templates *Nat. Nanotechnol.* **12** 244–50

[27] Kim T C *et al* 2018 Self-assembled multiferroic epitaxial $BiFeO_3$-$CoFe_2O_4$ nanocomposite thin films grown by RF magnetron sputtering *J. Mater. Chem.* C **6** 5552–61
[28] Wang Y *et al* 2017 Room temperature self-assembled growth of vertically aligned columnar copper oxide nanocomposite thin films on unmatched substrates *Sci. Rep.* **7** 11122
[29] Huang J, MacManus-Driscoll J L and Wang H 2017 New epitaxy paradigm in epitaxial self-assembled oxide vertically aligned nanocomposite thin films *J. Mater. Res.* **32** 4054–66
[30] Sun X, Macmanus-Driscoll J L and Wang H 2020 MR50CH10_MacManus-driscoll arjats.cls spontaneous ordering of oxide-oxide epitaxial vertically aligned nanocomposite thin films
[31] Zheng H *et al* 2004 Multiferroic $BaTiO_3$-$CoFe_2O_4$ nanostructures *Science* **303** 661–3
[32] Gao X, Li L, Jian J, Wang H, Fan M, Huang J, Wang X and Wang H 2018 Vertically aligned nanocomposite $BaTiO_3$:YMnO3 thin films with room temperature multiferroic properties toward nanoscale memory devices *ACS Appl. Nano Mater.* **1** 2509–14
[33] Zheng H, Wang J, Mohaddes-Ardabili L, Wuttig M, Salamanca-Riba L, Schlom D G and Ramesh R 2004 Three-dimensional heteroepitaxy in self-assembled $BaTiO_3$- $CoFe_2O_4$ nanostructures *Appl. Phys. Lett.* **85** 2035–7
[34] Zheng H, Straub F, Zhan Q, Yang P-L, Hsieh W-K, Zavaliche F, Chu Y-H, Dahmen U and Ramesh R 2006 Self-assembled growth of $BiFeO_3$-$CoFe_2O_4$ nanostructures *Adv. Mater.* **18** 2747–52
[35] Zheng H *et al* 2006 Controlling self-assembled perovskite — spinel nanostructures pp 1–7
[36] Huang J, Zhang D, Liu J and Wang H 2022 Freestanding $La_{0.7}Sr_{0.3}$ MnO_3 : niO vertically aligned nanocomposite thin films for flexible perpendicular interfacial exchange coupling
[37] Chen A, Bi Z, Hazariwala H, Zhang X, Su Q, Chen L, Jia Q, MacManus-Driscoll J L and Wang H 2011 Microstructure, magnetic, and low-field magnetotransport properties of self-assembled $(La_{0.7}Sr_{0.3}MnO_3)_{0.5}$:$(CeO_2)_{0.5}$ vertically aligned nanocomposite thin films *Nanotechnology* **22** 0–6
[38] Chen A *et al* 2014 Evolution of microstructure, strain and physical properties in oxide nanocomposite films *Sci. Rep.* **4** 1–7
[39] Tang X, Gao M, Luo H, Li J and Viehland D D 2020 Self-assembled patterned $CoFe_2O_4$-$SrRuO_3$ electrodes: enhanced functional properties by polar nano-regions reorientation *J. Am. Ceram. Soc.* **103** 3726–31
[40] Zhao R *et al* 2022 Emergent multiferroism with magnetodielectric coupling in $EuTiO_3$ created by a negative pressure control of strong spin-phonon coupling *Nat. Commun.* **13** 2364
[41] Merz W J 1956 Switching time in ferroelectric $BaTiO_3$ and its dependence on crystal thickness *J. Appl. Phys.* **27** 938–43
[42] Zi Z, Sun Y, Zhu X, Yang Z, Dai J and Song W 2009 Synthesis and magnetic properties of $CoFe_2O_4$ ferrite nanoparticles *J. Magn. Magn. Mater.* **321** 1251–5
[43] Liang R, Dosanjh P, Bonn D A, Baar D J, Carolan J F and Hardy W N 1992 Growth and properties of superconducting YBCO single crystals *Physica* C **195** 51–58
[44] Ouyang J *et al* 2023 Grain engineering of high energy density $BaTiO_3$ thick films integrated on Si *Microstructures* (https://doi.org/10.20517/microstructures.2023.22)
[45] Liu J, Wang X, Wang H, Qi Z, Barnard J P, Zhang B and Wang H 2022 Multiferroic self-assembled $BaTiO_3$-Fe vertically aligned nanocomposites on mica substrates toward flexible electronics *ACS Appl. Electron. Mater.* **4** 4077–84
[46] Liu J *et al* 2020 Multifunctional self-assembled $BaTiO_3$-Au nanocomposite thin films on flexible mica substrates with tunable optical properties *Appl. Mater. Today* **21** 100856
[47] Zhang D, Misra S, Jian J, Lu P, Li L, Wissel A, Zhang X and Wang H 2021 Self-assembled $BaTiO_3$-Au xAg1- xLow-loss hybrid plasmonic metamaterials with an ordered 'nano-domino-like' microstructure *ACS Appl. Mater. Interfaces* **13** 5390–8
[48] Zhang B *et al* 2020 Tunable, room-temperature multiferroic Fe-$BaTiO_3$ vertically aligned nanocomposites with perpendicular magnetic anisotropy *Mater. Today Nano* **11** 100083
[49] Huang J, Wang H, Qi Z, Lu P, Zhang D, Zhang B, He Z and Wang H 2021 Multifunctional metal-oxide nanocomposite thin film with plasmonic au nanopillars embedded in magnetic $La_{0.67}Sr_{0.33}MnO_3$Matrix *Nano Lett.* **21** 1032–9
[50] Zhang B, Huang J, Jian J, Rutherford B X, Li L, Misra S, Sun X and Wang H 2019 Tuning magnetic anisotropy in Co-$BaZrO_3$ vertically aligned nanocomposites for memory device integration *Nanoscale Adv.* **1** 4450–8
[51] Rutherford B X, Dou H, Zhang B, He Z, Barnard J P, Paldi R L and Wang H 2022 Single-step fabrication of Au-Fe-$BaTiO_3$ nanocomposite thin films embedded with non-equilibrium Au-Fe alloyed nanostructures *Nanomaterials* **12** 3460
[52] Liu J, Wang X, Gao X, Wang H, Zhang B, Zhang D, Kalaswad M, Huang J and Wang H 2022 Integration of self-assembled $BaZrO_3$-Co vertically aligned nanocomposites on mica substrates toward flexible spintronics *Cryst. Growth Des.* **22** 718–25
[53] Kalaswad M, Yang Y, Huang K-Y, Kong H J, Flick M J and Han B 2020 Tailorable Fe nanostructures and magnetic anisotropy in $(La_{0.5}Sr_{0.5}FeO_3)_{1-x}$:Fex thin films integrated on $SrTiO_3$ and silicon substrates *Mater. Today Adv.* **8** 100117
[54] Huang J, Zhang D, Qi Z, Zhang B and Wang H 2021 Hybrid Ag-$LiNbO_3$ nanocomposite thin films with tailorable optical properties *Nanoscale Adv.* **3** 1121–6
[55] Zhang D *et al* 2020 Tunable optical properties in self-assembled oxide-metal hybrid thin films via Au-phase geometry control: from nanopillars to nanodisks *Adv. Opt. Mater.* **8** 1–10
[56] Zhang D, Qi Z, Jian J, Huang J, Phuah X L, Zhang X and Wang H 2020 Thermally stable Au-$BaTiO_3$ nanoscale hybrid metamaterial for high-temperature plasmonic applications *ACS Appl. Nano Mater.* **3** 1431–7
[57] Li L *et al* 2016 Self-assembled epitaxial Au-oxide vertically aligned nanocomposites for nanoscale metamaterials *Nano Lett.* **16** 3936–43
[58] Song J *et al* 2024 Thermally stable 3D-metamaterial designs with advanced hyperbolic dispersion manipulation and magnetic anisotropy *Adv. Mater. Interfaces* **11** 2400132
[59] Song J, Zhang D, Lu P, Zhang Y, Wang H, Dou H, Xu X, Deitz J, Zhang X and Wang H 2023 Self-assembled complex three-phase core–shell nanostructure of Au–$CoFe_2$—TiN with a magneto-optical coupling effect *ACS Appl. Mater. Interfaces* **15** 37810–7
[60] Song J *et al* 2023 Anisotropic optical and magnetic response in self-assembled TiN–$CoFe_2$ nanocomposites *Mater. Today Nano* **22** 100316
[61] Kalaswad M *et al* 2022 TiN–Fe vertically aligned nanocomposites integrated on silicon as a multifunctional platform toward device applications *Crystals* **12** 849
[62] Wang X *et al* 2019 Self-assembled Ag–TiN hybrid plasmonic metamaterial: tailorable tilted nanopillar and optical properties *Adv. Opt. Mater.* **7** 1–9
[63] Wang X and Wang H 2020 Self-assembled nitride-metal nanocomposites: recent progress and future prospects *Nanoscale* **12** 20564–79
[64] Wang X *et al* 2019 Hybrid plasmonic Au-TiN vertically aligned nanocomposites: a nanoscale platform towards tunable optical sensing † *Nanoscale Adv.* **1** 1045–54

[65] Wang X, Wang H, Jian J, Rutherford B X, Gao X, Xu X, Zhang X and Wang H 2020 Metal-free oxide-nitride heterostructure as a tunable hyperbolic metamaterial platform *Nano Lett.* **20** 6614–22

[66] Naik G V, Saha B, Liu J, Saber S M, Stach E A, Irudayaraj J M K, Sands T D, Shalaev V M and Boltasseva A 2014 Epitaxial superlattices with titanium nitride as a plasmonic component for optical hyperbolic metamaterials *Proc. Natl Acad. Sci. USA* **111** 7546–51

[67] Yatsugi K and Nishikawa K 2019 Highly anisotropic titanium nitride nanowire arrays for low-loss hyperbolic metamaterials fabricated via dynamic oblique deposition *Nanotechnology* **30** 335705

[68] Guo W P, Mishra R, Cheng C-W, Wu B-H, Chen L-J, Lin M-T and Gwo S 2019 Titanium nitride epitaxial films as a plasmonic material platform: alternative to gold *ACS Photonics* **6** 1848–54

[69] Naik G V, Shalaev V M and Boltasseva A 2013 Alternative plasmonic materials: beyond gold and silver *Adv. Mater.* **25** 3264–94

[70] Guo Z, Jiang H and Chen H 2020 Hyperbolic metamaterials: from dispersion manipulation to applications *J. Appl. Phys.* **127** 071101

[71] Shekhar P, Atkinson J and Jacob Z 2014 Hyperbolic metamaterials: fundamentals and applications *Nano Convergence* **1** 14

[72] Maccaferri N, Zubritskaya I, Razdolski I, Chioar I-A, Belotelov V, Kapaklis V, Oppeneer P M and Dmitriev A 2020 Nanoscale magnetophotonics *J. Appl. Phys.* **127** 080903

[73] Fan B, Nasir M E, Nicholls L H, Zayats A V and Podolskiy V A 2019 Magneto-optical metamaterials: nonreciprocal transmission and faraday effect enhancement *Adv. Opt. Mater.* **7** 1801420

[74] Yoon J, Araujo R, Grunbaum N, Baqué L, Serquis A, Caneiro A, Zhang X and Wang H 2007 Nanostructured cathode thin films with vertically-aligned nanopores for thin film SOFC and their characteristics *Appl. Surf. Sci.* **254** 266–9

[75] Yoon J, Cho S, Kim J-H, Lee J, Bi Z, Serquis A, Zhang X, Manthiram A and Wang H 2009 Vertically aligned nanocomposite thin films as a cathode/electrolyte interface layer for thin-film solid oxide fuel cells *Adv. Funct. Mater.* **19** 3868–73

[76] Qi Z, Tang J, Misra S, Fan C, Lu P, Jian J, He Z, Pol V G, Zhang X and Wang H 2020 Enhancing electrochemical performance of thin film lithium ion battery via introducing tilted metal nanopillars as effective current collectors *Nano Energy* **69** 104381

[77] Qi Z, Jian J, Huang J, Tang J, Wang H, Pol V G and Wang H 2018 $LiNi_{0.5}Mn_{0.3}Co_{0.2}O_2$/Au nanocomposite thin film cathode with enhanced electrochemical properties *Nano Energy* **46** 290–6

[78] Dou H *et al* 2021 Electroforming-free HfO_2:CeO_2 vertically aligned nanocomposite memristors with anisotropic dielectric response *ACS Appl. Electron. Mater.* **3** 5278–86

[79] Dou H *et al* 2023 Self-assembled Au nanoelectrodes: enabling low-threshold-voltage HfO_2-based artificial neurons *Nano Lett.* **23** 9711–8

[80] Ohring M 1967 Materials science of thin film *Angew. Chem., Int. Ed.* **6** 951–2

[81] Molleman B and Hiemstra T 2018 Size and shape dependency of the surface energy of metallic nanoparticles: unifying the atomic and thermodynamic approaches *Phys. Chem. Chem. Phys.* **20** 20575–87

[82] Holec D, Dumitraschkewitz P, Vollath D and Fischer F D 2020 Surface energy of au nanoparticles depending on their size and shape *Nanomaterials* **10** 484

[83] Lekakh S N and Medvedeva N I 2015 Ab initio study of Fe adsorption on the (0 0 1) surface of transition metal carbides and nitrides *Comput. Mater. Sci.* **106** 149–54

[84] Owolabi T O, Akande K O and Olatunji S O 2017 Estimation of average surface energies of transition metal nitrides using computational intelligence technique *Soft Comput.* **21** 6175–82

[85] Vitos L, Ruban A V, Skriver H L and Kollár J 1998 The surface energy of metals *Surf. Sci.* **411** 186–202

[86] Westwood A R C and Goldheim D L 1963 Cleavage surface energy of {100} magnesium oxide *J. Appl. Phys.* **34** 3335–9

[87] Meyer B, Padilla J, Vanderbilt D and April R 1999 Theory of PbTiO, BaTiO, and SrTiO surfaces *Faraday Discuss.* **114** 395–405

[88] Zhang D and Wang H 2021 Self-assembled metal–dielectric hybrid metamaterials in vertically aligned nanocomposite form with tailorable optical properties and coupled multifunctionalities *Adv. Photon. Res.* **2** 2000174

[89] Wang X and Wang H 2021 Recent advances in vertically aligned nanocomposites with tunable optical anisotropy: fundamentals and beyond *Chemosensors* **9** 145

[90] Gao J, Wu X, Li Q, Du S, Huang F, Liang L, Zhang H, Zhuge F, Cao H and Song Y 2017 Template-free growth of well-ordered silver nano forest/ceramic metamaterial films with tunable optical responses *Adv. Mater.* **29** 1605324

[91] Mohaddes-Ardabili L *et al* 2004 Self-assembled single-crystal ferromagnetic iron nanowires formed by decomposition *Nat. Mater.* **3** 533–8

[92] Huang J *et al* 2018 Nanoscale artificial plasmonic lattice in self-assembled vertically aligned nitride–metal hybrid metamaterials *Adv. Sci.* **5** 1800416

[93] Kim D H, Aimon N M and Ross C A 2014 Pillar shape modulation in epitaxial $BiFeO_3$-$CoFe_2O_4$ vertical nanocomposite films *APL Mater.* **2** 081101

[94] Zhang W *et al* 2014 Strain relaxation and enhanced perpendicular magnetic anisotropy in $BiFeO_3$:$CoFe_2O_4$ vertically aligned nanocomposite thin films *Appl. Phys. Lett.* **104** 062402

[95] Shimada T, Arisue K, Wang J and Kitamura T 2014 *Ab initio* study of multiferroic $BiFeO_3$ (110) surfaces *Phys. Rev.* B **89** 1–9

[96] Chen A, Norouzi N, McLane J, Sharma H, Sharac N, Grant T, Chen A, Strayer S, Ragan R and Khine M 2013 Magnetotransport properties of quasi-one-dimensionally channeled vertically aligned heteroepitaxial nanomazes *Appl. Phys. Lett.* **102** 063504

[97] Sun X, Li Q, Huang J, Jian J, Lu P, Zhang X, MacManus-Driscoll J L and Wang H 2019 Strain and property tuning of the 3D framed epitaxial nanocomposite thin films via interlayer thickness variation *J. Appl. Phys.* **125** 082530

[98] Enriquez E *et al* 2020 Induced ferroelectric phases in $SrTiO_3$ by a nanocomposite approach *Nanoscale* **12** 18193–9

[99] Rutherford B X, Zhang B, Wang X, Sun X, Qi Z, Wang H and Wang H 2020 Strain effects on the growth of $La_{0.7}Sr_{0.3}MnO_3$(LSMO)-NiO nanocomposite thin films via substrate control *ACS Omega* **5** 23793–8

[100] Zhao R *et al* 2014 Precise tuning of $(YBa_2Cu_3O_{7-\delta})_{1-x}$:$(BaZrO_3)_x$ thin film nanocomposite structures *Adv. Funct. Mater.* **24** 5240–5

[101] Huang J *et al* 2021 Core-shell metallic alloy nanopillars-in-dielectric hybrid metamaterials with magneto-plasmonic coupling *Mater. Today* **51** 39–47

[102] Huang J *et al* 2020 3D hybrid plasmonic framework with Au nanopillars embedded in nitride multilayers integrated on Si *Adv. Mater. Interfaces* **7** 1–9

[103] Weng X *et al* 2022 Strain-engineering of magnetic anisotropy in Cox Ni_{1-x}-$SrTiO_3$/$SrTiO_3$ (001) vertically assembled nanocomposites *Phys. Rev. Mater.* **6** 046001

[104] Hennes M *et al* 2020 Structural, vibrational, and magnetic properties of self-assembled CoPt nanoalloys embedded in $SrTiO_3$ *Phys. Rev. Mater.* **4** 126001

[105] Huang J, Zhang D and Wang H 2021 Epitaxial TiN/MgO multilayers with ultrathin TiN and MgO layers as hyperbolic metamaterials in visible region *Mater. Today Phys.* **16** 100316
[106] He Z, Jian J, Misra S, Gao X, Wang X, Qi Z, Yang B, Zhang D, Zhang X and Wang H 2020 Bidirectional tuning of phase transition properties in Pt: VO_2 nanocomposite thin films *Nanoscale* **12** 17886–94
[107] Huang J *et al* 2018 Tailorable optical response of Au–$LiNbO_3$ hybrid metamaterial thin films for optical waveguide applications *Adv. Opt. Mater.* **6** 1800510
[108] Shen J, He Z, Zhang D, Lu P, Deitz J, Shang Z, Kalaswad M, Wang H, Xu X and Wang H 2022 Tunable physical properties in Bi-based layered supercell multiferroics embedded with Au nanoparticles *Nanoscale Adv.* **4** 3054–64
[109] Misra S, Li L, Zhang D, Jian J, Qi Z, Fan M, Chen H-T, Zhang X and Wang H 2019 Self-assembled ordered three-phase Au–$BaTiO_3$—ZnO vertically aligned nanocomposites achieved by a templating method *Adv. Mater.* **31** 1–8
[110] Wang X *et al* 2021 Nitride-oxide-metal heterostructure with self-assembled core–shell nanopillar arrays: effect of ordering on magneto-optical properties *Small* **17** 2007222
[111] Tyson W R and Miller W A 1977 Surface free energies of solid metals: estimation from liquid surface tension measurements *Surf. Sci.* **62** 267–76
[112] de Boer F R, Mattens W C M, Boom R, Miedema A R and Niessen A K 1988 *Cohesion in Metals : Transition Metal Alloys* (available at: https://www.osti.gov/etdeweb/biblio/5556327)
[113] Ahmad A, Peng J, SharafEldin K, Lu J, Wang H and El-Azab A 2024 A DFT-based kinetic Monte Carlo simulation of multiphase oxide-metal thin film growth *J. Appl. Phys.* **135** 095307
[114] Wang G, Sun F, Zhou S, Zhang Y, Zhang F, Wang H, Huang J and Zheng Y 2024 Enhanced memristive performance via a vertically heterointerface in nanocomposite thin films for artificial synapses *ACS Appl. Mater. Interfaces* **16** 12073–84
[115] Huang J, Wang H, Wang X, Gao X, Liu J and Wang H 2020 Exchange bias in a $La_{0.67}Sr_{0.33}MnO_3$/NiO heterointerface integrated on a flexible mica substrate *ACS Appl. Mater. Interfaces* **12** 39920–5
[116] Huang J, Zhang D, Liu J, Dou H and Wang H 2021 Double-exchange bias modulation under horizontal and perpendicular field directions by 3D nanocomposite design *ACS Appl. Mater. Interfaces* **13** 50141–8
[117] Zhu H, Tang Z, Wang G, Fang Y, Huang J and Zheng Y 2023 Memristive artificial synapses based on Au-TiO_2 composite thin film for neuromorphic computing *APL Mater.* **11** 061103
[118] Zhang D, Kalaswad M and Wang H 2022 Self-assembled vertically aligned nanocomposite systems integrated on silicon substrate: progress and future perspectives *J. Vac. Sci. Technol.* A **40** 010802
[119] Kalaswad M, Zhang D, Gao X, Contreras L L, Wang H, Wang X and Wang H 2019 Integration of hybrid plasmonic Au-$BaTiO_3$ metamaterial on silicon substrates *ACS Appl. Mater. Interfaces* **11** 45199–206
[120] Shen J, Tsai B K, Xu K, Shang A, Barnard J P, Zhang Y, Tripathi R, Chen Z, Zhang X and Wang H 2023 A generalized synthesis method for freestanding multiferroic two-dimensional layered supercell oxide films via a sacrificial buffer layer *Nano Res.* **16** 10559–66
[121] Tsai B K, Song J, Liu J, Shen J, Zhang Y, Zhang X and Wang H 2024 Au nanopillar array prepared by selective etching of Au-$Sr_3Al_2O_6$ vertically aligned nanocomposite thin films *Next Nanotechnol.* **6** 100071